

Article

Broadband Right-Angle Rectangular Waveguide to Substrate Integrated Waveguide Transition with Distributed Impedance Matching Network

Roberto Vincenti Gatti * , Riccardo Rossi  and Marco Dionigi

Department of Engineering, University of Perugia, 06125 Perugia, Italy;
rickbrk@hotmail.it (R.R.); marco.dionigi@unipg.it (M.D.)

* Correspondence: roberto.vincentigatti@unipg.it; Tel.: +39-075-585-3671

Received: 20 December 2018; Accepted: 21 January 2019; Published: 23 January 2019



Featured Application: hybrid beam forming networks for phased array antennas.

Abstract: A broadband right-angle rectangular waveguide to substrate integrated waveguide transition for hybrid RWG-SIW (rectangular waveguide–substrate integrated waveguide) feeding networks is presented. The narrower return loss bandwidth issue with respect to in-line configurations is addressed with the introduction of a multi-section matching network consisting of a number of symmetric E-plane irises in the rectangular waveguide section. A hybrid design procedure based on circuit simulation and full-wave optimization is outlined and adopted to synthesize three matching networks with respectively one, two, and three irises, according to the bandwidth to be covered. The design procedure is experimentally validated with a proof-of-concept prototype.

Keywords: rectangular waveguide; substrate integrated waveguide; waveguide transition

1. Introduction

A high-gain pencil beam radiation pattern, often required in satellite communications and radar systems, can be synthesized by large planar arrays. These antennas, where hundreds of radiating elements are arranged, show appealing features such as low profile and light weight [1]. However, the insertion loss due to the feeding networks long electrical paths causes radiation efficiency and gain degradations. One promising approach to reduce such loss is to divide the planar array into modules where microwave power is delivered by a low-loss hybrid feeding network. This can be made of planar circuits such as substrate integrated waveguides (SIWs), grounded coplanar waveguides (GCPWs) or quasi-planar structures such as air-filled rectangular waveguides (RWGs), connected together with low-loss transitions.

SIWs have received much attention in recent years [2,3]. It consists of two rows of periodic holes embedded in a dielectric substrate, electrically connecting two parallel metal plates. Some advantages of SIW technology include low loss, high Q-factor, low profile, light weight, high-density integration with planar circuits, low cost, and easy fabrication with standard printed circuit board (PCB) technology.

On the other hand, the traditional RWG, due to the absence of the dielectric substrate, features a much lower insertion loss especially at high frequency bands and a higher power handling capability. Moreover, even if the SIW can potentially replace the RWG in some applications, a large number of commercial and existing products are in waveguide format, thus an RWG interface is anyway needed. Finally, RWGs are more rigid and therefore more suitable for the design of complex 3D feeding structures.

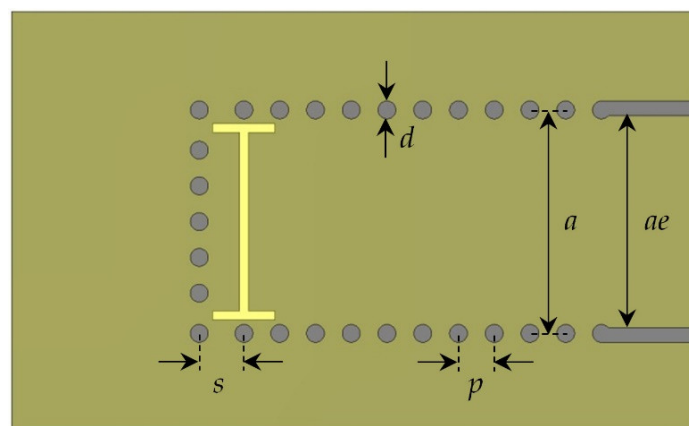
In hybrid feeding networks both the SIW and RWG technologies are employed, thus a broadband and low-loss transition is necessary in order to connect the two transmission lines. There are two main geometrical configurations for RWG-to-SIW transitions, namely the in-line and the right-angle configurations, which differ from one another because of the longitudinal axes of both waveguides being respectively collinear or perpendicular. In-line transitions [4–11] use probes or probes together with waveguide tapers and exhibit wide bandwidths at the expense of bulky volumes, thus making this geometry not suitable when compactness is required. Moreover, in-line transitions are not compatible with subarraying in the specific scenario of antenna arrays based on a tile architecture. For these reasons, right-angle transitions may also be required. Such configurations employ a coupling aperture etched on the broad wall of the SIW, leading to greater compactness and good system layout, at the expense of narrower bandwidths.

The coupling aperture comes in the form of a single slot in [12], which is designed according to slotted waveguide theory. Bandwidth is limited due to the slot resonant behavior, though it can be improved using a pair of slots resonating at two close frequencies as in [13]. Slot-to-slot coupling between the SIW and the RWG ground planes is employed in [14], but again the frequency range is still limited for many applications. The slots bandwidth can be extended with the same principle of aperture-coupled patch antennas by introducing additional substrate layers with printed parasitic patches [15,16]. Wider bandwidths can be found in [17–19], where transitions are matched by means of properly shaped apertures, stepped ridges, and SIW inductive posts. The most broadband performance can be obtained when the device is designed similarly to an E-plane waveguide bend: Very good matching is ensured by a stepped transition region where the steps are realized with additional substrate layers [20] or integrated in the RWG flange [21].

In this paper a novel right-angle RWG-to-SIW transition is presented, which makes use of a distributed impedance matching network, in the form of symmetric E-plane irises. Bandwidth performance depends on the number of matching elements introduced. A prototype is manufactured with stereolithography (SLA) technology and then electroplated. Good agreement between simulated and measured results is observed. Circuit and full-wave simulations are respectively performed with the commercial software NI AWR (AWR Microwave Office 9 by National Instruments) Microwave Office and CST Microwave Studio (CST Microwave Studio 2015 by Dassault Systems).

2. Transition Design

The transition configuration consists of a standard WR75 waveguide connected perpendicularly to a SIW through a H-shaped coupling slot etched in the SIW bottom ground plane, as shown in Figure 1. The SIW top ground plane is hidden for better clarity.



(a)

Figure 1. Cont.

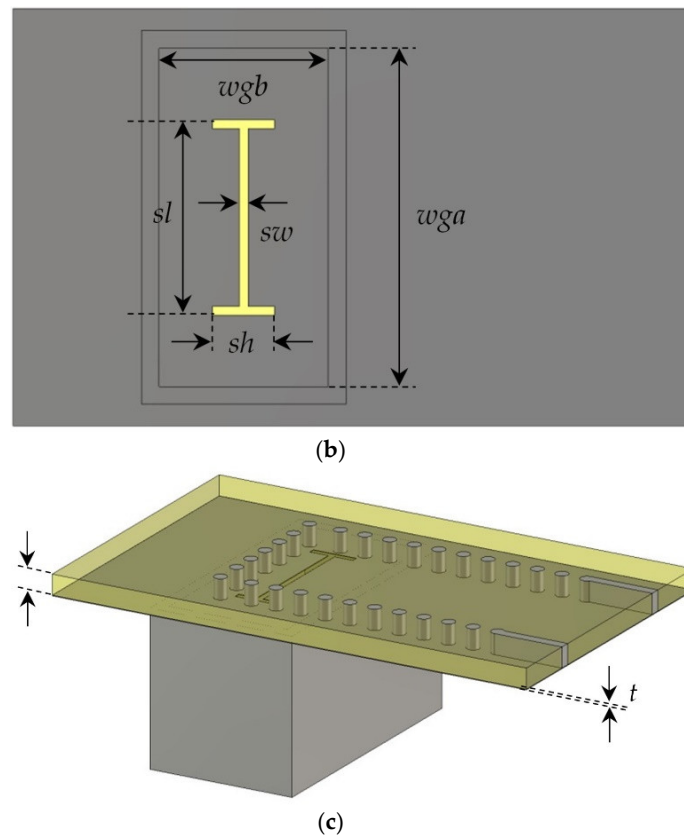


Figure 1. RWG-to-SIW transition geometry with no matching elements. (a) Top view; (b) Bottom view; (c) 3D view.

The characteristic impedance and the propagation constant of this SIW were equal to a dielectric-filled RWG with an equivalent width ae and the same height, as explained in [22,23]. The other edge of the SIW ends with a short circuit at a distance s , which was kept fixed for reasons to be discussed in the next section. Also, the slot dimensions remained unchanged and were optimized in order to maximize the transmission coefficient to the SIW with no matching elements. The H-shaped slot could be seen as a short double-ridge waveguide section and its cut-off frequency, equal to 9.15 GHz, was low enough to let the electromagnetic field propagate between the two transmission lines. A 2:1 hole pitch-to-diameter ratio was chosen for a reliable manufacturing. To minimize the insertion loss, the adopted substrate was RT5880 by Rogers Corporation, with a dielectric constant $\epsilon_r = 2.2$ and $\tan\delta = 0.001$ measured at 10 GHz. The substrate height was $b = 1.575$ mm and the metal thickness was $t = 35 \mu\text{m}$, though it was increased to $45 \mu\text{m}$ in the design to include the effects of the metal hole deposition in a following manufacturing process. The design center frequency was around 12.5 GHz and the simulation bandwidth was between 10 to 15 GHz, which is the typical operating frequency range for a WR75 waveguide. The transition geometrical parameters and simulated scattering parameters are presented in Table 1 and Figure 2. The RWG and the SIW are respectively indicated with port indices 1 and 2.

It is evident that, with no matching elements included, such transition exhibits poor return loss performance and cannot be utilized in hybrid feeding networks for large planar array antennas. It is worth mentioning that similar performance would be obtained with any other slot shape, given the fact that the equivalent load connected to the RWG presents a very low impedance, tending towards a short circuit when the substrate thickness becomes very small. Nevertheless, the thinner the slot width sw , the higher is the transmission coefficient. In addition to that, by adopting an H-shaped slot, the return loss at the RWG port can be further improved. In Figure 2 the scattering parameters obtained with a standard rectangular slot ($sh = sw$, dashed lines) and the optimized H-shaped slot (solid lines)

are compared. An improvement of about 1 dB in the return loss can be observed. The transition with the H-shaped slot therefore represents a good starting point for the design of a distributed impedance matching network. The latter can be realized by a number of symmetric irises carved in the RWG E-plane, as depicted in Figure 3. Each iris is specified by its height h and its width w . Without loss of generality, a constant iris width equal to $w = 1$ mm was adopted. A blending radius $br = 1.25$ mm was considered to ease a fabrication process in the case of CNC (computer numerical control) milling machine manufacturing.

Table 1. RWG-to-SIW transition geometrical parameters.

Parameter	Description	Value (mm)
a	SIW width	12.500
ae	Equivalent RWG width	11.865
d	Via hole diameter	1.000
p	Via hole pitch	2.000
s	Short distance	2.500
b	Substrate height	1.575
t	Metal thickness	0.045
sl	Slot length (vertical)	11.000
sh	Slot length (horizontal)	3.500
sw	Slot width	0.500
wga	RWG width	19.050
wgb	RWG height	9.525

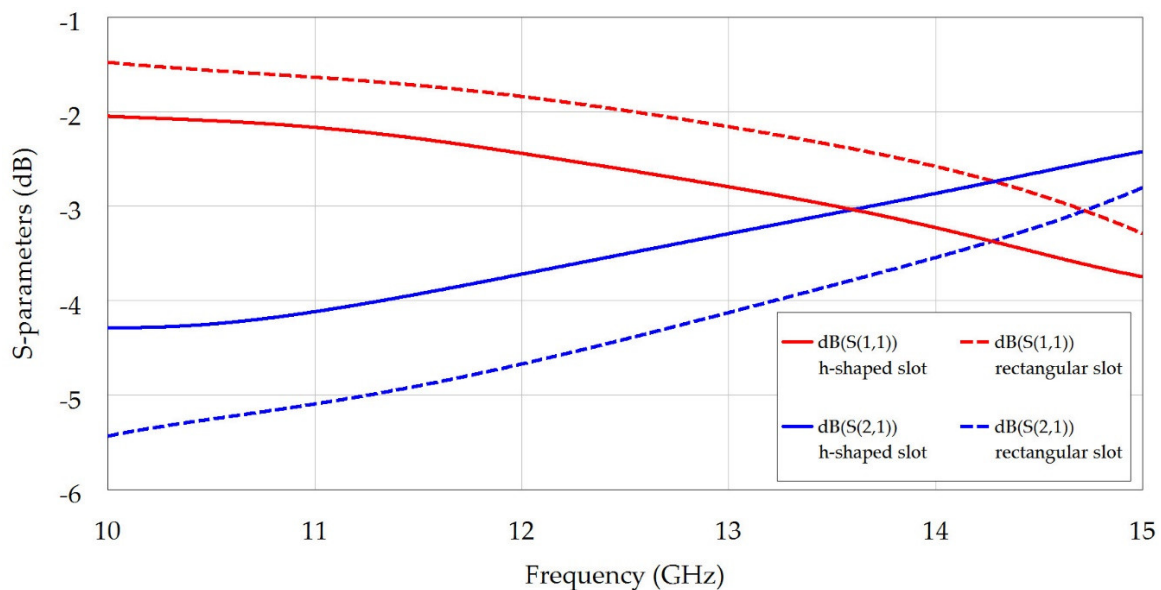


Figure 2. RWG-to-SIW transition simulated scattering parameters (no matching elements).

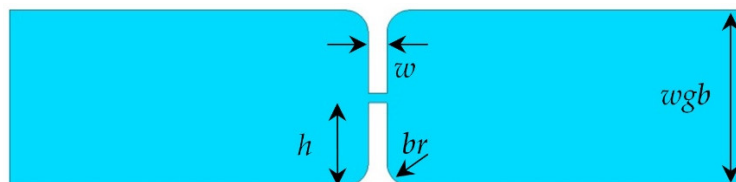


Figure 3. RWG symmetric E-plane iris (side view, air inside metallic background).

Wideband matching can be achieved with multi-section matching networks, which can be quickly synthesized with the aid of a circuit simulation software. On the other hand, a full-wave simulation software can accurately predict the performance of an electromagnetic structure, at the expense of

increased computational cost. Since a complete full-wave design of a matching network with more than one iris would be extremely time-consuming and convergence could not be ensured, the idea was to perform a hybrid synthesis using both simulators. In particular, a proper equivalent circuit associated to the iris geometrical parameters was extracted and then employed in the design of a wideband matching network at a circuit level, and finally the output geometrical parameters were used in the full-wave design. Note that a circuit simulation does not take into account potential higher order modes interactions, thus a final full-wave optimization may be necessary. Anyway, given this first estimate, this process would lead to a very good return loss performance quite rapidly.

It is well known from waveguide theory that a symmetric E-plane iris can be schematized as an equivalent shunt capacitance [24,25], but this statement holds true only in a neighborhood of the center frequency. As a consequence, such circuits cannot accurately predict the iris behavior in terms of scattering parameters over the large bandwidth required in many applications and, for this reason, another model must be derived. In this design the iris is to be characterized when its height h , which is the only varying parameter, is swept from 0.5 mm to 4.5 mm with a step of 0.5 mm. A total of nine scattering matrices are extracted from full-wave simulations and, for each geometrical configuration, it can be verified from circuit simulations that a suitable broadband modeling of the iris can be achieved by introducing a lumped shunt inductance. The equivalent circuit is shown in Figure 4.

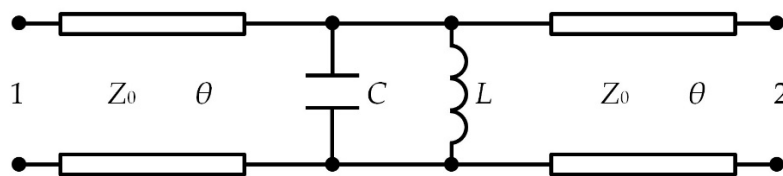


Figure 4. Symmetric E-plane iris equivalent circuit.

It consists of one capacitance C and one inductance L connected so as to form a shunt LC resonator. In addition to this, two identical transmission lines with normalized impedance $Z_0 = 1$ and electrical length θ are introduced to account for second order contributions to the phase of the electric field. For each sampled iris configuration, defined by the parameter h , an optimization of the three circuit element values C , L , and θ , is to be performed so that the scattering matrix of the equivalent circuit fits the corresponding one from the full-wave simulation over a wide bandwidth. The fitting procedure results are listed in Table 2.

Table 2. Equivalent circuit parameters for the iris configurations.

Iris Height (mm)	C (pF)	L (pH)	θ (deg)
0.500	1.776	314.162	-0.512
1.000	3.838	165.103	-1.526
1.500	6.438	100.696	-2.192
2.000	10.131	63.611	-2.765
2.500	14.894	44.643	-3.374
3.000	22.089	29.057	-4.039
3.500	31.240	22.417	-4.537
4.000	49.427	14.315	-5.198
4.500	110.015	6.473	-5.883

The proposed equivalent circuit performance for a selected iris geometry are reported in Figure 5, both in magnitude and phase, and compared with the standard shunt capacitance model. A very good agreement was verified on a 40% fractional bandwidth. It is worth mentioning that this wideband fitting cannot be obtained with the standard single-element model.

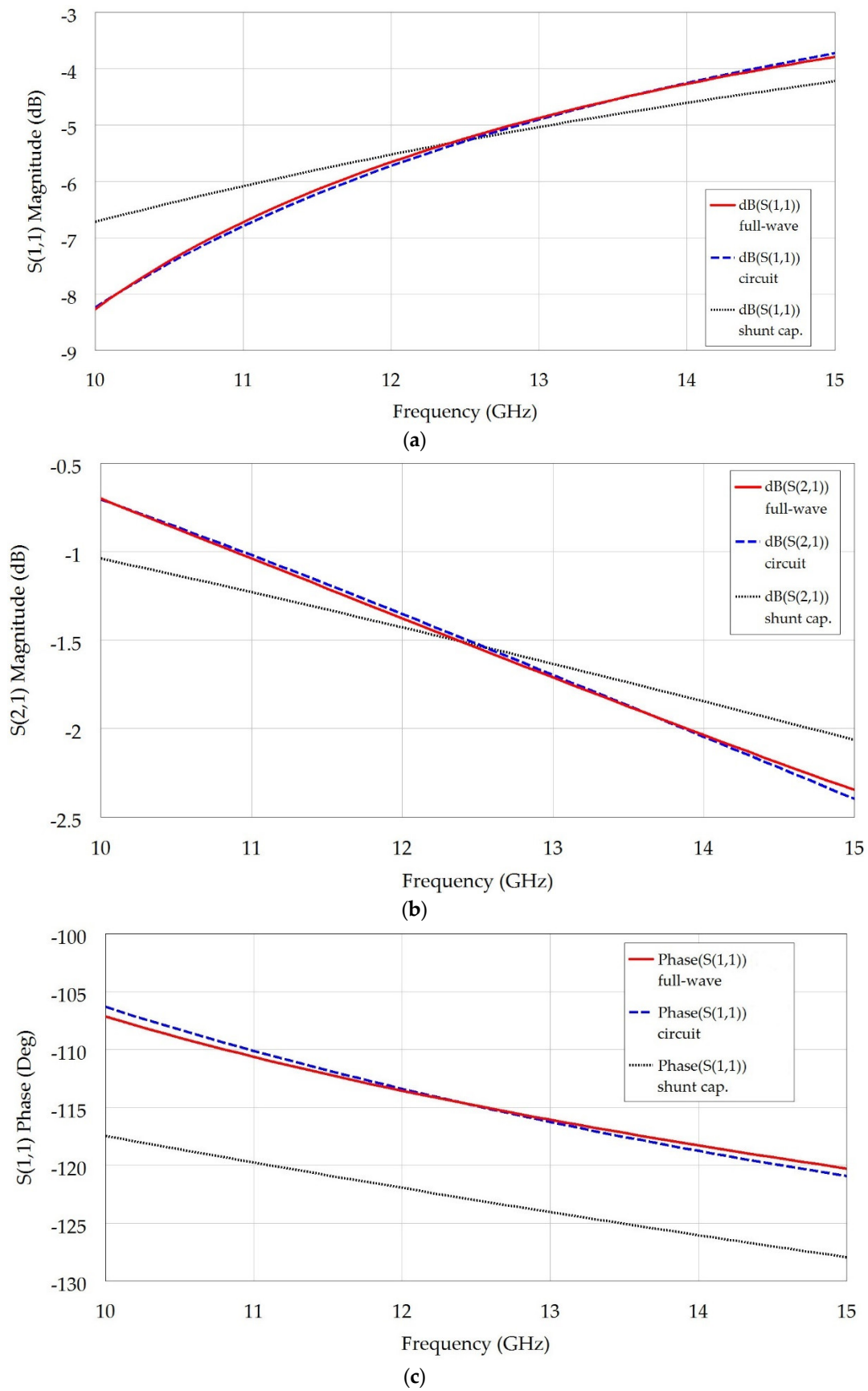


Figure 5. Cont.

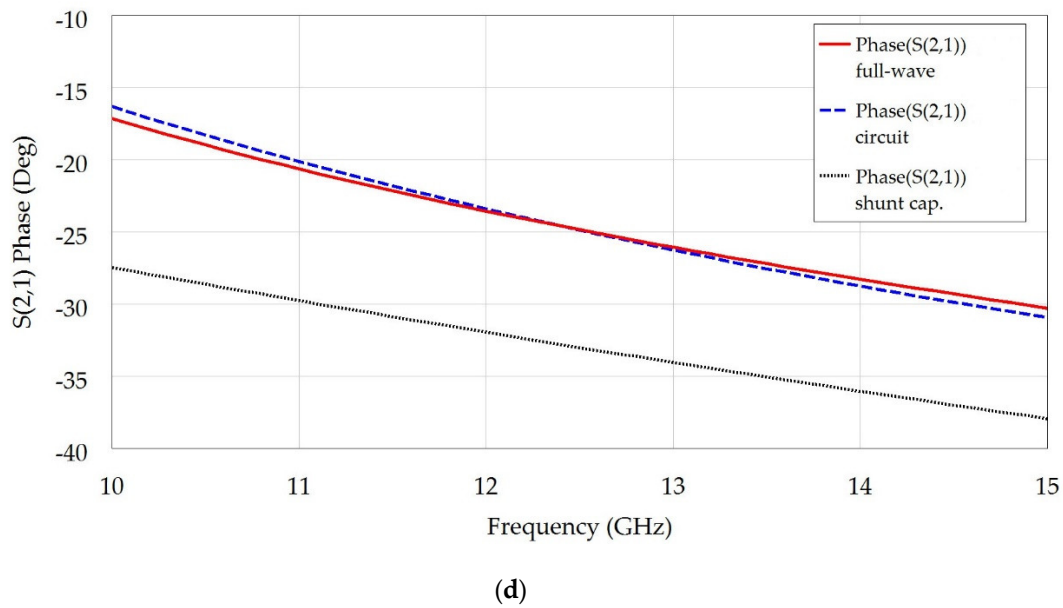


Figure 5. Symmetric E-plane iris scattering parameters for $h = 3$ mm. (a) $|S_{11}|$; (b) $|S_{21}|$; (c) $\angle S_{11}$; (d) $\angle S_{21}$.

A least-squares polynomial interpolation of the computed circuit element values was to be performed to have an estimate of the iris scattering matrices for any height value in the above mentioned range. The fitting polynomial grades were selected to be $n = 3$ for each parameter as a trade-off between interpolation accuracy and computational cost in the following design stage. Fitting polynomials for C , L , and θ were:

$$C(h) = \frac{c_3h^3 + c_2h^2 + c_1h + c_0}{h - 4.7625} \tag{1}$$

$$L(h) = l_3h^3 + l_2h^2 + l_1h + l_0 \tag{2}$$

$$\theta(h) = t_3h^3 + t_2h^2 + t_1h + t_0 \tag{3}$$

Note that (1) differs from the cubic curves (2) and (3) because of a vertical asymptote given by the geometrical upper limit for the iris height, which completely shorts the waveguide when $h = wgb/2$. Once the interpolation coefficients c_i , l_i , and t_i are calculated, Equations (1)–(3) can be easily implemented in any circuit simulation software and scattering matrices with an accuracy close to that of a full-wave simulator can be obtained. The polynomial coefficients and interpolation results are respectively shown in Table 3 and Figure 6 for completeness sake.

Table 3. Polynomial interpolation coefficients for the circuit element values C , L , and θ .

Interpolation Coefficients			
c_3	c_2	c_1	c_0
1.364	−6.294	−4.894	−4.044
l_3	l_2	l_1	l_0
−12.950	126.500	−413.900	482.100
t_3	t_2	t_1	t_0
−0.051	0.428	−2.319	0.503

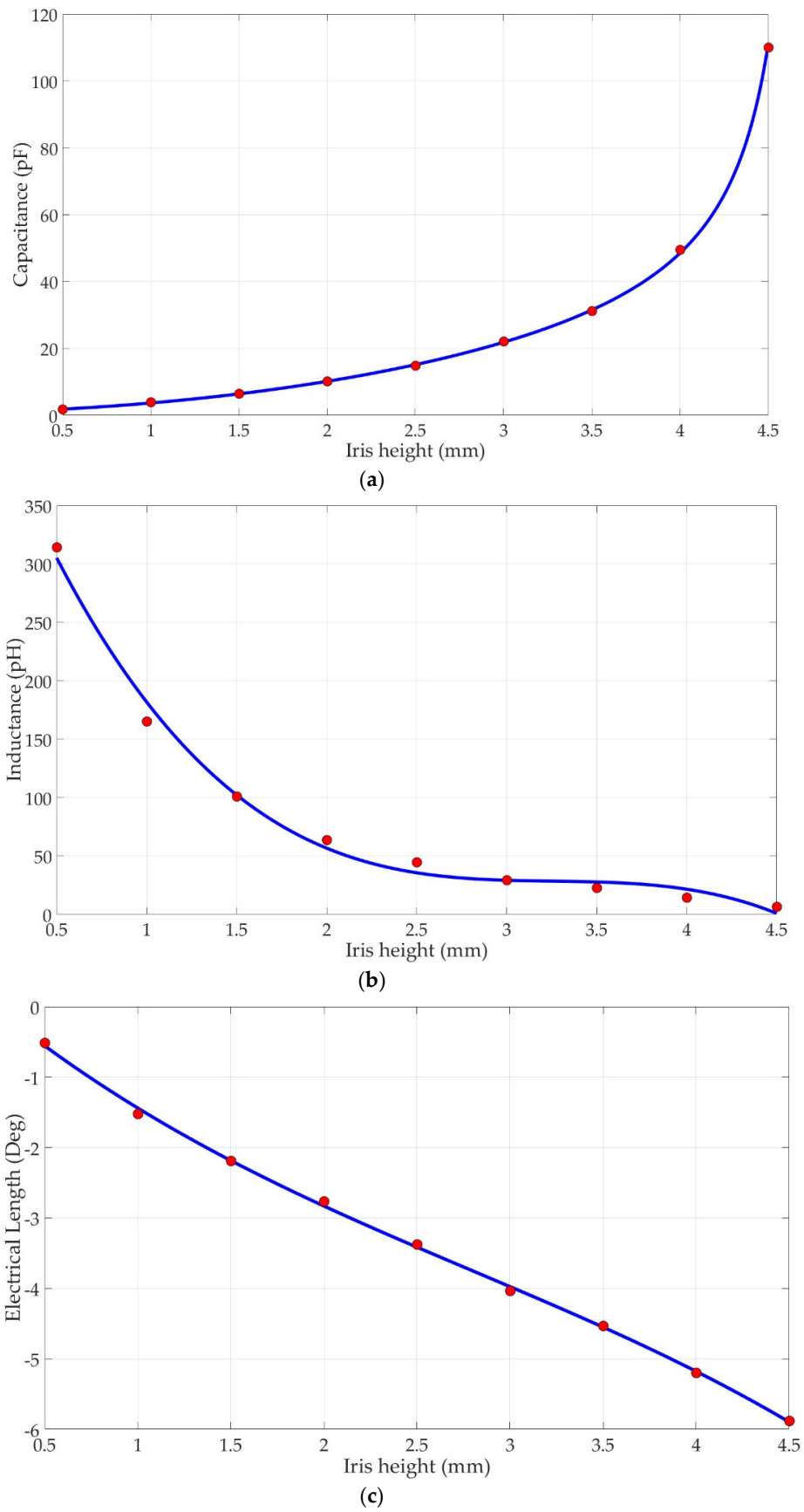


Figure 6. Fitting values (red dots) and polynomial interpolation (solid line) for the circuit element parameters. (a) C ; (b) L ; (c) θ .

At this point, the design of a multi-section matching network was straightforward. The subcircuits representing single irises were cascaded and separated by short RWG sections, modeled as transmission lines with normalized impedance $Z_0 = 1$ and electrical lengths $\theta_i = \beta L_i$, where β is the propagation constant calculated with classical waveguide theory [24,25] and L_i is the specific section physical length. A two-section matching network is presented in Figure 7 as an example: In particular, the circuit representation and physical implementation are illustrated.

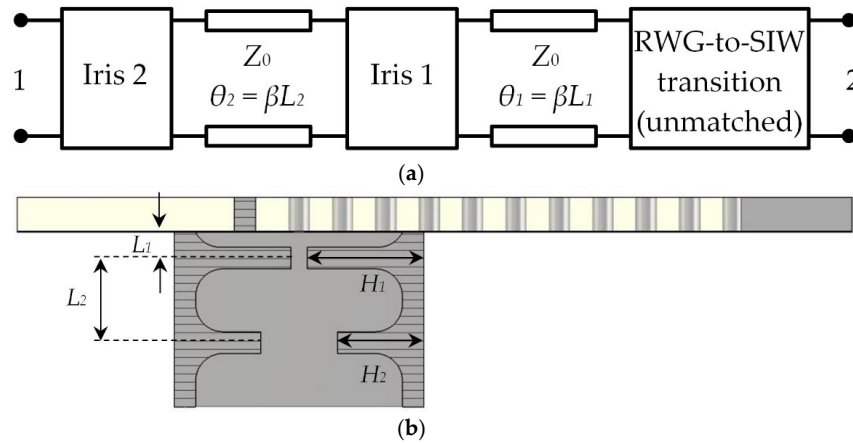


Figure 7. Two-section matching network. (a) Equivalent circuit; (b) Physical implementation.

Three matching networks including one, two, and three irises were designed with the circuit simulator to obtain the largest 20-dB return loss bandwidth. Once the irises heights and waveguide sections physical lengths were calculated, corresponding full-wave simulations were carried out to verify the agreement. Geometrical parameters are listed in Table 4 and a comparison between circuit and full-wave simulated scattering parameters are reported in Figure 8.

Table 4. Matching networks geometrical parameters.

Parameter	Description	Network 1 Value (mm)	Network 2 Value (mm)	Network 3 Value (mm)
H_1	First iris height	3.595	4.199	4.381
H_2	Second iris height	-	2.945	3.848
H_3	Third iris height	-	-	2.329
L_1	First iris distance	2.220	1.482	1.181
L_2	Second iris distance	-	3.950	2.892
L_3	Third iris distance	-	-	5.110

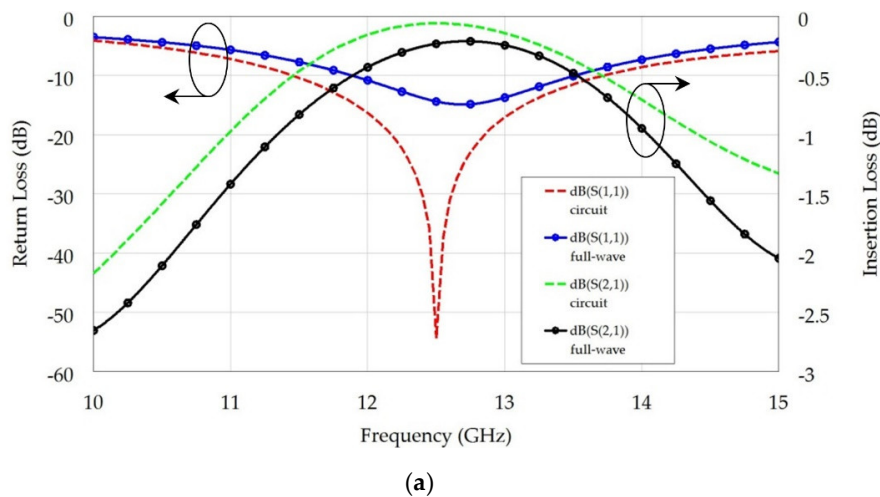


Figure 8. Cont.

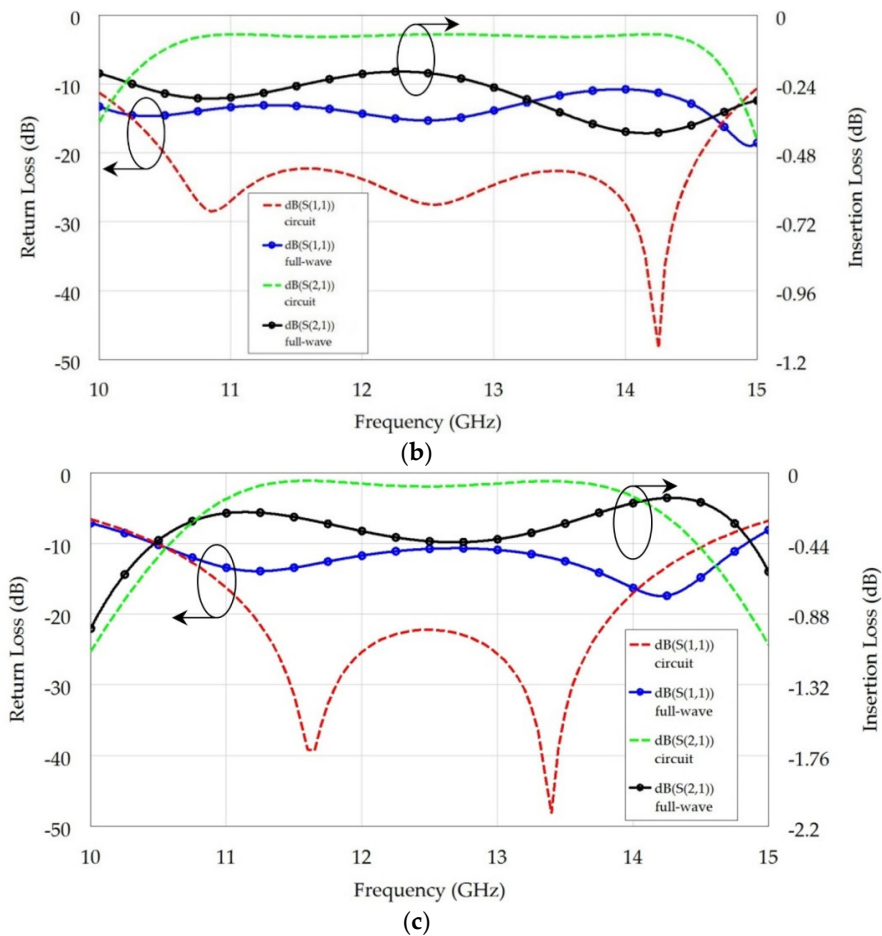
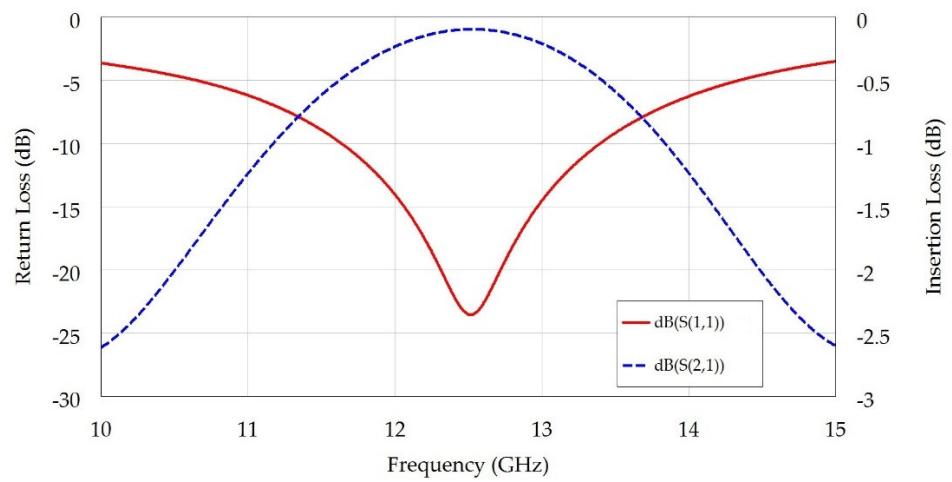


Figure 8. Circuit and full-wave simulated scattering parameters for three matching networks. (a) One iris; (b) Two irises; (c) Three irises.

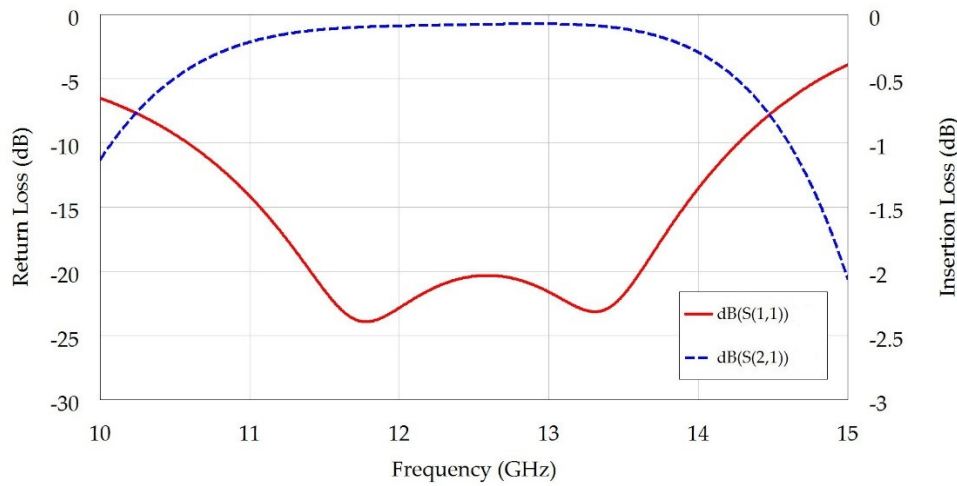
The discrepancy between circuit and full-wave curves is to be imputed to higher order modes that are excited in the waveguide sections between adjacent irises and near the coupling slot and were not taken into account in this simple unimodal circuit simulation. Such modes degrade the return loss levels and, in the third case, a resonance disappears. A final full-wave optimization was therefore necessary, but the computational effort was considerably eased since optimum values were close to the starting one calculated previously. This is the great advantage of the presented method, which resides in the implementation of the model in a circuit simulation software, leading to a quicker matching network design when compared to a pure full-wave solution. Optimized matching networks parameters and simulated scattering parameters are shown in Table 5 and Figure 9.

Table 5. Matching networks optimized geometrical parameters.

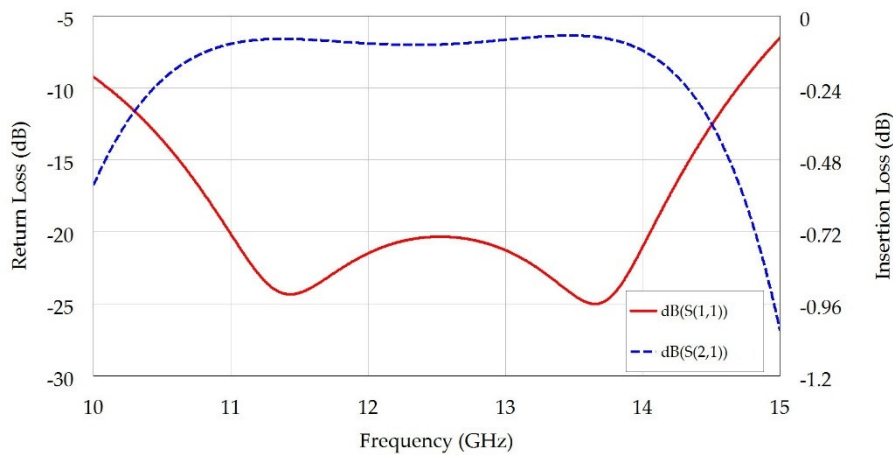
Parameter	Description	Network 1 Value (mm)	Network 2 Value (mm)	Network 3 Value (mm)
H_1	First iris height	3.815	4.378	4.475
H_2	Second iris height	-	3.002	3.780
H_3	Third iris height	-	-	1.681
L_1	First iris distance	1.998	1.174	0.912
L_2	Second iris distance	-	3.881	2.910
L_3	Third iris distance	-	-	5.181



(a)



(b)



(c)

Figure 9. Full-wave simulated scattering parameters for three optimized matching networks. (a) One iris; (b) Two irises; (c) Three irises.

The 20-dB return loss bandwidth improves with an increasing number of irises. Fractional bandwidths of 3.28%, 17.59%, and 24.51% were obtained in the three cases. Insertion loss was better than 0.2 dB and flatter in the frequency ranges corresponding to good input port matching.

A comparison in terms of bandwidth and dimensions between this device and right-angle RWG-to-SIW transitions in referenced works [12–21] is presented in Table 6. All geometrical parameters refer to the SIW. In particular, the SIW height (i.e. the substrate thickness) is defined as fractions of the cut-off wavelength $\lambda_c = 2a_e\sqrt{\epsilon_r}$ in the ratio r . As the substrate thickness decreases, the SIW broad walls get closer to one another. The lower the ratio r the lower the SIW section input impedance, and as a consequence the harder is to obtain good matching over a wide band. To perform a fair comparison between the various solutions reported in the literature [12–21] the bandwidth performance are therefore normalized with the introduction of the merit factor $F = BW_{20dB}/r$. It is worth mentioning that simulated results for standalone transitions are reported, in order to provide a comparison among data not affected by manufacturing errors in the fabricated prototypes.

Table 6. Comparison between RWG-to-SIW transitions in referenced works.

Reference	f_0 (GHz)	ϵ_r	a (mm)	b (mm)	ae (mm)	λ_c (mm)	$r = b/\lambda_c$ (%)	20-dB BW (%)	Merit Factor $F = BW_{20dB}/r$
[12]	34.90	2.20	5.25	0.508	5.05	14.98	3.39	1.15	0.34
[13]	26.00	3.40	6.05	1.905	5.78	21.32	8.93	5.83*	0.65
[14]	29.75	3.55	4.80	0.787	4.54	17.12	4.60	3.36	0.73
[15]	92.50	3.50	1.30	0.254	1.18	4.40	5.77	11.89	2.06
[16]	65.00	2.20	2.66	0.787	2.32	6.88	11.44	23.08	2.01
[17]	33.25	2.20	5.30	0.787	4.90	14.55	5.41	38.81	7.17
[18]	36.00	2.20	5.00	0.508	4.62	13.71	3.71	16.67	4.49
[19]	34.90	2.20	4.30	1.575	3.91	11.58	13.60	25.22	1.85
[20]	18.38	2.20	8.40	0.787	8.01	23.77	6.62	27.37	4.13
[21]	31.50	2.20	5.20	1.575	4.80	14.25	11.05	64.52	5.83
This work	12.53	2.20	12.5	1.575	11.87	35.17	4.48	24.51	5.47

* 15-dB BW (%).

Though the fractional bandwidth of the present work is not the largest among the list of referenced papers, the high performance of the proposed solution becomes evident when considering also the ratio r and the merit factor F .

3. Transition Manufacturing and Test

The single-iris version was selected for experimental validation because of its higher robustness with respect to manufacturing tolerances. To ease the manufacturing process the RWG was split into two blocks, fabricated with a Form 2 SLA printer by Formlabs and metalized with a two-step process consisting of silver painting followed by electrolytic copper deposition in a copper sulfide solution. Electrical contact between the two manufactured parts was provided by screws. Further details on this SLA additive manufacturing and metallization are discussed in [26]. This process was adopted in order to minimize time and costs and has exhibited good results for other proof-of-concept prototypes [27,28]. The SIW circuit was manufactured with standard PCB technology and then connected to the RWG, the latter being integrated in a mechanical support structure with mounting screws tightened in six holes drilled in the PCB. A GCPW feeding section for port 2 was preferred over a microstrip line because of a reduced insertion loss due to spurious radiation and a lower influence with the RWG mechanical support. In addition to this, it was easy to integrate a GCPW transmission line with a K-type solder-less connector adopted for the measurements, which is the 2.92-mm jack (female) end-launch connector model 1092-03A-5 by Southwest Microwave. A SIW-to-GCPW transition was designed according to [29] and included in the following simulations. In particular, a properly dimensioned tapered section converts the frequency-dependent SIW impedance to the GCPW 50- Ω port impedance with a return loss better than 20 dB in the bandwidth of interest. The SIW-to-GCPW transition geometry, simulated performance, and geometrical parameters are respectively reported in Figure 10 and Table 7.

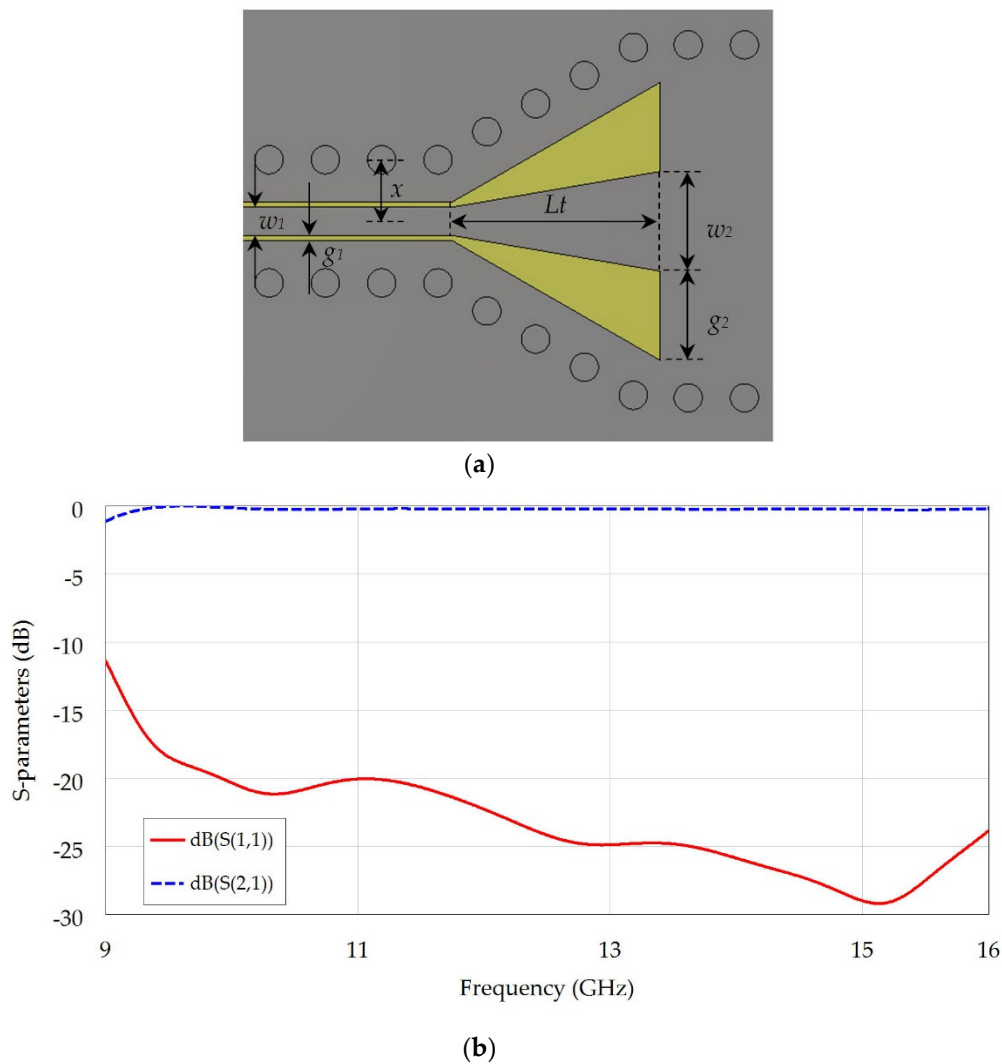


Figure 10. SIW-to-GCPW transition. (a) Geometry. (b) Simulated scattering parameters.

Table 7. SIW-to-GCPW transition geometrical parameters.

Parameter	Description	Value (mm)
w_1	GCPW initial width	1.00
w_2	GCPW final width	3.53
g_1	GCPW initial gap	0.18
g_2	GCPW final gap	3.16
L_t	Taper length	7.39
x	Line-via distance	2.18

A complete prototype is shown in Figure 11a after the assembly. In Figure 11b the fabricated RWG is open to visualize the internal details. The prototypes were tested with an Agilent N5230A vector network analyzer using the well-known full two-port short-open-load-through calibration technique. Measured performances are reported in Figure 12 and compared to simulated results. Physical properties of copper conductivity and material roughness were taken into account in the simulation. In particular, an estimated metallic roughness on the order of 5 μm contributed to deteriorate copper conductivity. A de-embedding procedure was also applied to the measured results in order to remove the effects of the coaxial connector as in [30], relying on the datasheet and measured data provided by the manufacturer. The estimated insertion loss for the connector is approximately 0.4 dB at 10 GHz and 0.5 dB at 15 GHz.

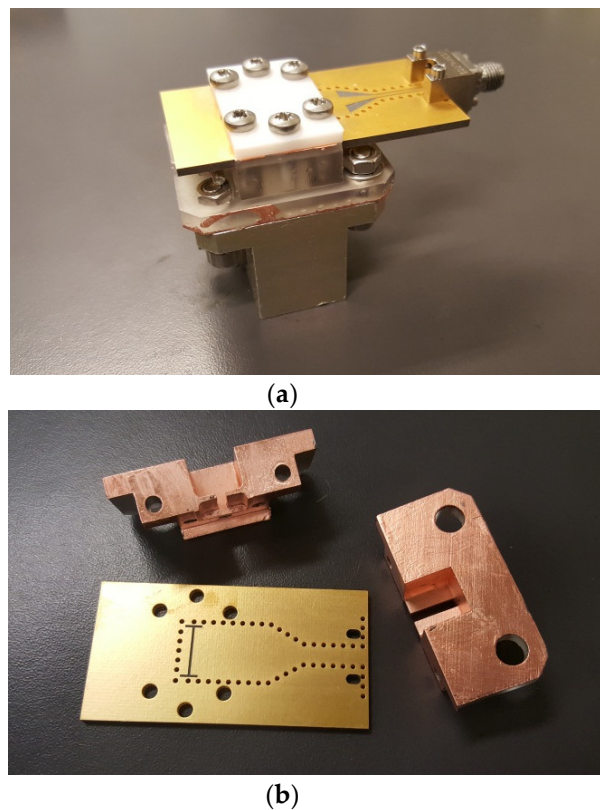


Figure 11. RWG-to-SIW transition prototype. (a) Assembled structure; (b) Matching networks details. PCB size is 29 × 56 mm.

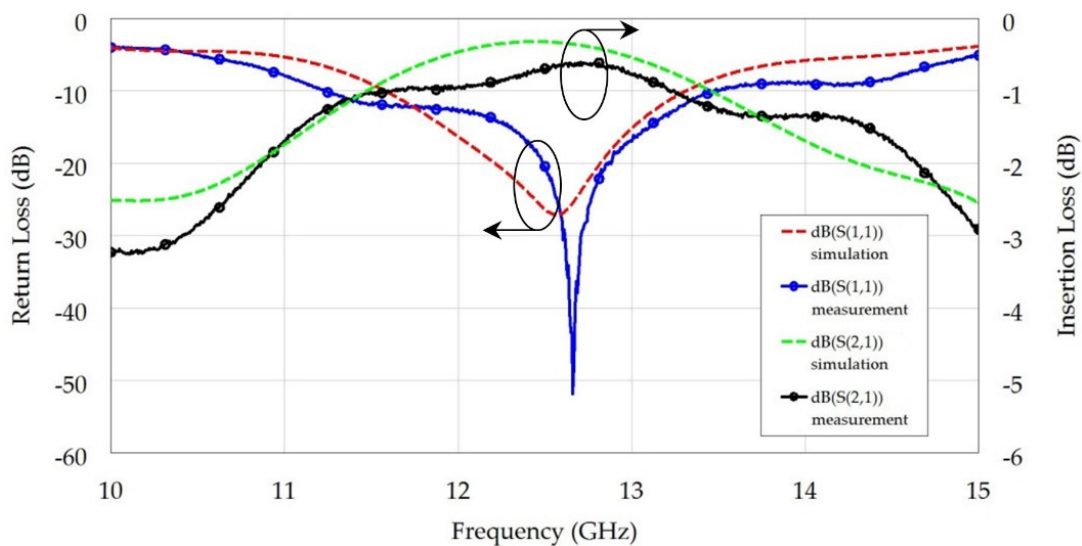


Figure 12. RWG-to-SIW transition scattering parameters for single-iris matching network.

Measured results showed a good agreement with simulations, though a small frequency shift in the return loss and a slightly larger insertion loss were observed. Discrepancies in the return loss can be explained by a 0.1-mm fabrication tolerance associated with the SLA manufacturing, misalignment errors and plastic deformation in the assembling. The increased insertion loss was due to a poor electric contact between the PCB and 3D-printed RWG section. The same device, manufactured in aluminum with a CNC milling machine and assembled with standard industrial processes, would have improved the agreement between simulated and measured results, at the expense of higher costs.

Nevertheless, measured curves are indicative of good performance for the mentioned fast in-house fabrication process.

4. Conclusions

In this work a broadband right-angle rectangular waveguide to substrate integrated waveguide transition has been presented. The proposed solution is particularly useful in all applications where hybrid RWG-SIW architectures are employed, such as active phased arrays and beam forming networks. Broadband performance with a low-profile SIW substrate has been achieved with the introduction of a multi-section matching network consisting of a number of symmetric E-plane irises in the RWG section. The design procedure made use of equivalent circuits for the single iris, then were combined to model the whole network in order to reduce the computational cost with respect to a pure full-wave synthesis. Simulated 20-dB return loss fractional bandwidths of 3.28%, 17.59%, and 24.51% were obtained respectively for the single, double and triple-iris matching networks for a PCB with thickness equal to 4.5% of the cut-off wavelength. The design procedure has been experimentally validated with a proof-of-concept prototype based on SLA technology, obtaining good agreement with simulations.

Author Contributions: Conceptualization, R.V.G.; supervision, R.V.G.; software, R.R.; writing—original draft preparation, R.R.; writing—review and editing, R.V.G. and R.R.; validation, M.D.

Funding: This research received no external funding.

Acknowledgments: The authors would like to thank P. Mezzanotte at the DI, University of Perugia, Perugia, Italy, for his support in the measurement setup and device test.

Conflicts of Interest: The authors declare no conflict of interest.

References

1. Vincenti Gatti, R.; Marcaccioli, L.; Sbarra, E.; Sorrentino, R. Flat Array Antenna for Ku-Band Mobile Satellite Terminals. In Proceedings of the IEEE 5th European Conference Antennas and Propagation, Rome, Italy, 11–15 April 2011.
2. Deslandes, D.; Wu, K. Integrated microstrip and rectangular waveguide in planar form. *IEEE Microw. Wireless Comp. Lett.* **2001**, *11*, 68–70. [[CrossRef](#)]
3. Deslandes, D.; Wu, K. Single-substrate integration technique of planar circuits and waveguide filters. *IEEE Trans. Microw. Theory Tech.* **2003**, *51*, 593–596. [[CrossRef](#)]
4. Xia, L.; Xu, R.; Yan, B.; Li, J.; Guo, Y.; Wang, J. Broadband transition between air-filled waveguide and substrate integrated waveguide. *IET Electron. Lett.* **2003**, *42*, 1403–1405. [[CrossRef](#)]
5. Li, Z.; Chen, X.P.; Wu, K. A Surface Mountable Pyramidal Horn Antenna and Transition to Substrate Integrated Waveguide. In Proceedings of the IEEE International Symposium on Signals, System and Electronics, Montreal, QC, Canada, 30 July–2 August 2007. [[CrossRef](#)]
6. Zhong, C.L.; Xu, J.; Zhi, Z.Y.; Jin, C.X. Broadband substrate integrated waveguide to rectangular waveguide transition with fin-line. *IET Electron. Lett.* **2009**, *45*, 205–207. [[CrossRef](#)]
7. Li, J.; Wen, G.; Xiao, F. Broadband transition between rectangular waveguide and substrate integrated waveguide. *IET Electron. Lett.* **2010**, *46*, 223–224. [[CrossRef](#)]
8. Dousset, D.; Wu, K.; Claude, S. Millimetre-wave broadband transition of substrate-integrated waveguide to rectangular waveguide. *IET Electron. Lett.* **2010**, *46*, 1610–1611. [[CrossRef](#)]
9. Jin, H.; Chen, W.; Wen, G. Broadband transition between waveguide and substrate integrated waveguide based on quasi-yagi antenna. *IET Electron. Lett.* **2012**, *48*, 355–356. [[CrossRef](#)]
10. Cano, J.L.; Mediavilla, A.; Perez, A.R. Full-band air-filled waveguide-to-substrate integrated waveguide (SIW) direct transition. *IEEE Microw. Wireless Comp. Lett.* **2014**, *25*, 79–81. [[CrossRef](#)]
11. Lee, H.; Yun, S.; Uhm, M.; Yom, I. Full-band transition from substrate integrated waveguide to rectangular waveguide. *IET Electron. Lett.* **2015**, *51*, 1089–1090. [[CrossRef](#)]
12. Li, L.; Chen, X.; Khazaka, R.; Wu, K. A Transition from Substrate Integrated Waveguide (SIW) to Rectangular Waveguide. In Proceedings of the IEEE Asia Pacific Microwave Conference, Singapore, 7–10 December 2009.

13. Glogowski, R.; Zurcher, J.F.; Peixeiro, C.; Mosig, J.R. Broadband ka-band rectangular waveguide to substrate integrated waveguide transition. *IET Electron. Lett.* **2013**, *49*, 602–604. [[CrossRef](#)]
14. Abdel-Wahab, W.M.; Ehsandar, A.; Al-Saedi, H.; Safavi-Naeini, S. E-plane metallic rwg-to-siw transition for large-scale mm-wave phased array antenna applications. *IET Electron. Lett.* **2016**, *52*, 1465–1467. [[CrossRef](#)]
15. Zhang, D.; Xu, Z.; Xiao, Y.; Sun, H. A Wideband SIW-to-Waveguide Transition at W-Band. In Proceedings of the IEEE Sixth Asia Pacific Conference Antennas and Propagation, Xi'an, China, 16–19 October 2017. [[CrossRef](#)]
16. Li, Y.; Luk, K.M. A broadband v-band rectangular waveguide to substrate integrated waveguide transition. *IEEE Microw. Wireless Comp. Lett.* **2014**, *24*, 590–592. [[CrossRef](#)]
17. Dong, J.; Yang, Z.; Peng, H.; Yang, T. Full ka-band right-angle transition from substrate integrated waveguide to air-filled rectangular waveguide. *IET Electron. Lett.* **2015**, *51*, 1796–1798. [[CrossRef](#)]
18. Zhang, G.; Yi, H.; Wang, S.; Han, M. Broadband right-angle transition from substrate integrated waveguide to rectangular waveguide. *IET Electron. Lett.* **2017**, *53*, 473–475. [[CrossRef](#)]
19. Li, T.; Dou, W. Broadband right-angle transition from substrate-integrated waveguide to rectangular waveguide. *IET Electron. Lett.* **2014**, *50*, 1355–1356. [[CrossRef](#)]
20. Jankovic, U.; Budimir, D. Stepped Bend Substrate Integrated Waveguide to Rectangular Waveguide Transitions. In Proceedings of the IEEE International Symposium Antennas and Propagation, Fajardo, PR, 26 June–1 July 2016. [[CrossRef](#)]
21. Li, T.; Dou, W.; Meng, H. Wideband Transition between Substrate Integrated Waveguide (Siw) and Rectangular Waveguide (Rwg) based on bend waveguide. In Proceedings of the IEEE Asia Pacific Microwave Conference, Sendai, Japan, 4–7 November 2014.
22. Yan, L.; Hong, W.; Wu, K.; Cui, T.J. Investigations on the propagation characteristics of the substrate integrated waveguide based on the method of lines. *IET Proc. Microw. Antennas Propag.* **2005**, *152*, 35–42. [[CrossRef](#)]
23. Vincenti Gatti, R.; Dionigi, M.; Sorrentino, R. Low cost active scanning antenna for mobile satellite terminals. In Proceedings of the IEEE Antennas and Propagation Society International Symposium Digest, Columbus, OH, USA, 22–27 June 2003. [[CrossRef](#)]
24. Pozar, D.M. *Microwave Engineering*, 4th ed.; John Wiley & Sons: Hoboken, NJ, USA, 2011.
25. Collin, R.E. *Foundations for Microwave Engineering*, 2nd ed.; (Series on Electromagnetic Wave Theory); IEEE Press: Hoboken, NJ, USA, 2000.
26. Dionigi, M.; Tomassoni, C.; Venanzoni, G.; Sorrentino, R. Simple high-performance metal-plating procedure for stereolithographically 3-d-printed waveguide components. *IEEE Microw. Wireless Comp. Lett.* **2017**, *27*, 953–955. [[CrossRef](#)]
27. Vincenti Gatti, R.; Rossi, R.; Dionigi, M. X-band right-angle coaxial-to-single ridge waveguide compact transition with capacitive coupling. *IET Electron. Lett.* **2018**. [[CrossRef](#)]
28. Vincenti Gatti, R.; Rossi, R.; Dionigi, M. In-line stepped ridge coaxial-to-rectangular waveguide transition with capacitive coupling. *Wiley Int. J. RF Microw. Comp. Aid. Eng.* **2018**, e21626. [[CrossRef](#)]
29. Kazemi, R.; Fathy, A.E.; Yang, S.; Sadeghzadeh, R.A. Development of an Ultra Wide Band GCPW to SIW Transition. In Proceedings of the IEEE Radio Wireless Symposium, Santa Clara, CA, USA, 15–18 January 2012. [[CrossRef](#)]
30. Vincenti Gatti, R.; Rossi, R. Hermetic broadband 3-dB power divider/combiner in substrate-integrated waveguide (SIW) technology. *IEEE Trans. Microw. Theory Tech.* **2018**, *66*, 3048–3054. [[CrossRef](#)]

